Full Feedforward of Grid Voltage for Discrete State Feedback Controlled Grid-Connected Inverter With *LCL* Filter

Mingyu Xue, Yu Zhang, *Member, IEEE*, Yong Kang, Yongxian Yi, Shuming Li, and Fangrui Liu

***Abstract*—Due to multifeedback of state variables, a discrete state-space controller offers outstanding control bandwidth as well as control stability for popular *LCL*-type grid-connected inverters, while the grid current is still vulnerable to the grid-voltage harmonics. The feedforward of grid voltage, usually employed in continuous controllers to solve such a problem, is too complicated to be applied for the discrete state-space controller. By means of continuous transformation, a full grid-voltage feedforward (GVFF) decoupling strategy is successfully proposed in this paper to make the feedforward possible for the discrete state-space controller. Based on the transfer function analysis and comparison of discretized and continuous system, comprehensive verification is also provided to verify the effectiveness of the derivation of the GVFF path. Subsequently, the robustness analysis of the proposed strategy to the grid impedance is also performed. Moreover, a grid-voltage estimator instead of the measured voltage is employed for the full GVFF, which not only retains the important information of grid voltage but also eliminates the influence of accompanied noises. The distinct features of the proposed feedforward controller plus implementation strategy are the super steady waveform, dynamic response, and robustness to the variation of grid impedance. Besides, the complexity of the algorithm is moderate and the computational burden is not significantly increased. Finally, simulation and experimental results are provided to verify the feasibility and validity of the proposed strategy.**

***Index Terms*—Continuous transformation, discrete state feedback, feedforward, *LCL* filter, robust.**

I. Introduction

VOLTAGE-SOURCE pulsewidth modulation (PWM) grid-connected converters [1] are widely used in modern industry, where renewable energy generation is of particular concern. To pursue green power as well as to meet the stringent harmonic standard, conventional *L* filter is replaced by the *LCL* filter, for better harmonic elimination capability. However, this brings challenges to suppress the *LCL* resonance.

Due to the additional power losses, passive damping [2] has been gradually substituted by the active ones. The capacitor voltage lead-lag compensation method proposed in [3] and [4] requires fine tuning to compensate the phase at the turn point of *LCL* filter and leads to a higher overshoot. A strategy of injecting oscillation in antiphase is proposed in [5]. The capacitor current feedback methods are presented in [6]–[9], of which, the method in [6] is based on the idea of dual loops, and methods in [7] and [9] are based on the idea of virtual resistor. The weighted-average-current feedback control method presented in [10] is to obtain the equivalent control plant of first order. However, the reference and feedback are not of the same quantity, thereby necessitating compensation. A notch filter is employed in cascade in [11], whereas complicated inheritance method is required to achieve adaptiveness and robustness. Among all of these strategies, the capacitor current feedback is prevalent.

The *LCL*-type inverter works well in most conditions with active damping; however, the stability fades under conditions of low resonance frequency and weak grid with relatively large impedance [3], [12]. Furthermore, condition like low-voltage ride through puts more stress on the dynamics. It indicates that to stabilize the system is insufficient. From the pole point of view, the potential instability results from the imperfect pole placement, due to shortage of freedom degrees. Thus, the bandwidth and stability margin are in contradiction. As is well known, higher bandwidth brings faster response, while larger stability margin introduces less overshoot. The multifeedback is, therefore, necessary to obtain adequate freedom degrees for ideal pole placement. In [13]–[15], the authors proposed some system design methods based on discrete state-space theory, which are able to achieve high bandwidth and suitable stability margin simultaneously. Another merit is that the design is standard and straightforward, thereby getting rid of any trial and error. However, such a controller takes charge of reference tracking only, while the coupling of grid-voltage current is actually more complicated due to the multifeedback.

The proportional resonant plus harmonic compensator controller (PR+HC) [16] is good at suppressing the grid background harmonics; however, its main drawbacks are the following: 1) the computational burden increases with the number of harmonics concerned; 2) only harmonic within the bandwidth is able

Manuscript received September 16, 2011; revised November 11, 2011 and January 26, 2012; accepted February 23, 2012. Date of current version May 31, 2012. This work was supported by the Natural Science Foundation of China under Award 51007026, Award 50837003, and Award 50877032, and by the Key Program of Delta Power Electronics Science and Education Development Plan (DREK2010002). Recommended for publication by Associate Editor M. Ponce-Silva.

M. Xue, Y. Zhang, Y. Kang, and Y. Yi are with the State Key Laboratory of Advanced Electromagnetic Engineering and Technology, Huazhong University of Science and Technology, Wuhan 430074, China (e-mail: mysure1984@gmail.com; zyu1126@mail.hust.edu.cn; ykang@mail.hust.edu.cn; cnyyx@sina.com).

S. Li is with the Zhicheng Champion Ltd., Guangdong 523718, China (e-mail: lsm@zhicheng-champion.com).

F. Liu is with the State Key Laboratory of Advanced Electromagnetic Engineering and Technology, Huazhong University of Science and Technology, Wuhan 430074, China, and also with Ryerson University, Toronto, ON M5B 2K3, Canada (e-mail: fangruihust@163.com).

Color versions of one or more of the figures in this paper are available online at http://ieeexplore.ieee.org.

Digital Object Identifier 10.1109/TPEL.2012.2190524

to be dealt with; and 3) the intended dynamics alters, usually slows down. All these give rise to grid-voltage decoupling by feedforward, which is to incorporate the variation of the grid voltage in the control through an additional feedforward path. Single proportional grid-voltage feedforward (GVFF) is usually enough for *L*-type grid interface, but not for *LCL*'s, where the disturbance path is of high order, requiring the GVFF path to be of the same order. An approximate full GVFF with converter current controlled is provided in [17], and a startup impedance specification by GVFF is presented in [18]. It is noticeable that the full GVFF method proposed in [9] offers attractive grid rejection ability, whereas it is effective for the case of active damping with capacitor-current feedback only. Moreover, system delay is neglected and stiff grid is assumed as well. A more generalized full GVFF method for discrete state-space controller remains undeveloped yet.

The system expressed by the shift operator z is so complicated that cumbers the establishment of full GVFF path. In addition, the differentiator in z-plane is not as evident as that in s-domain, where a single s is intuitively interpreted as d/dt. A further recognition is that a digital setup runs obeying its physical nature only, no matter whether discrete or continuous controller is applied. All make it rational to transform the discrete controlled system to be continuous, which is for the first time proposed and accomplished in this paper, by mapping the presentation of the inverter-grid formed system, from discrete state space into its continuous counterpart. The main benefit of this method, namely continuous transformation, lies in its generality: the system employing any type of discrete controller—active damping based on filter or based on multiloop [19], inverter current controlled or grid current controlled, rectifier or inverter, and even with active damping or with passive damping, the grid-voltage-current coupling can be unveiled explicitly, while a modification of the controller simply implies finding another one. Based on that, this paper successfully proposes a full GVFF decoupling strategy for discrete state feedback controller, particularly when grid current is directly injected into the grid. Such full GVFF path represents an extension to the existing ones.

Although the state-space controller has reserved considerable stability margin for grid impedance variation, the unsuitable implement of GVFF will on the other way lead to degradation of current control performance or loss of stability. A deep insight unveils that the major cause is the accompanied noise when performing the GVFF. Such noise includes the common-mode noise that can be reduced rather than eliminated by common-mode filter, and the sensitive information of grid current, which is induced by grid impedance and then is reflected in the sensed grid voltage, hence is absorbed in the main control loop through the GVFF to affect the dynamics of the main control loop. Considering the GVFF strategy involves two parts as grid voltage and path, which contains multiordered differentiators, it is necessary for either a noise immune but accuracy realization of path, or a "clean" grid voltage.

With respect to the path realization, to the authors' knowledge, a common solution is to employ a first-order low-pass filter (LPF) for each order of differentiator, while the sensed grid voltage is kept as another part of GVFF. However, the phase lag introduced by the LPF will seriously ruin the accuracy. Thus, it is so challenging to design an accurate but noise-immune differentiator that the sensed grid voltage is not suitable to be adopted directly. A "clean" grid voltage can then be restored for substitution. As one possible solution, the Kalman filter [14] can be employed to filter the grid voltage, except that the model of each grid harmonic voltage is required; thus, the number of concerned harmonic voltage is limited by the computational burden. In addition, Rodriguez *et al.* employ the adaptive band-pass filter (ABPF) for an advanced grid synchronization [20], while the ABPFs can, at the same time, serve to estimate the grid voltage. However, it encounters the same problem of computational burden as with the Kalman filter. Thus, unless such a grid synchronization method has been adopted already, the ABPFs should not be practical. In contrast, the grid-voltage estimator (GVE) provided in [21] is able to inherently capture a clean grid voltage that highly resembles the actual one, with fixed and low computational burden. It is thus promising to implement the full GVFF with GVE instead of the measured one, hence to allow pure differentiator to ensure accuracy. Moreover, this paper develops a phase compensator for GVE to further improve the performance.

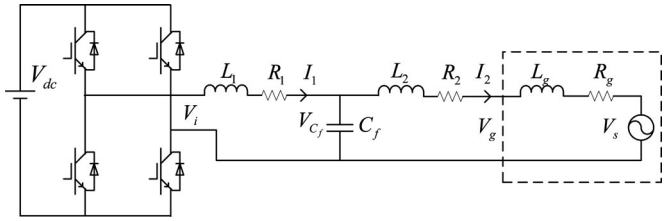

Fig. 1. Single-phase grid-connected inverter with *LCL* filter.

System modeling and discrete state-space control strategy are presented in Section II, followed by the corresponding continuous transformation as well as the establishment of the full GVFF path in Section III. Then, analysis of stability with GVFF, as well as the robust but accuracy implementation, is performed in Section IV. Finally, simulation and experimental results are provided in Sections V and VI, respectively, to verify the validity of the proposed strategy.

II. System Modeling and Discrete State-Space Control

A single-phase grid-connected inverter is shown in Fig. 1 where the dc link can be simplified as a battery with constant voltage of $V_{\rm dc}$ and the grid internal impedance as L_g and R_g are considered as well. From the relationship between the system input and output, the following modeling can be carried out.

A. Modeling in s-Domain

Take the state vector as $x = [\, I_1 \quad V_{C_f} \quad I_2 \,]^T$, the input vector as $u = [\, V_i \quad V_g \,]^T$ (V_i is the inverter output voltage that can be derived from the duty cycle), and the output vector as $C = [\, 0 \quad 0 \quad 1 \,]$—grid current is set as control object. Provided that the variables in the following equations are normalized, the continuous state-space equation can be derived by Kirchhoff's

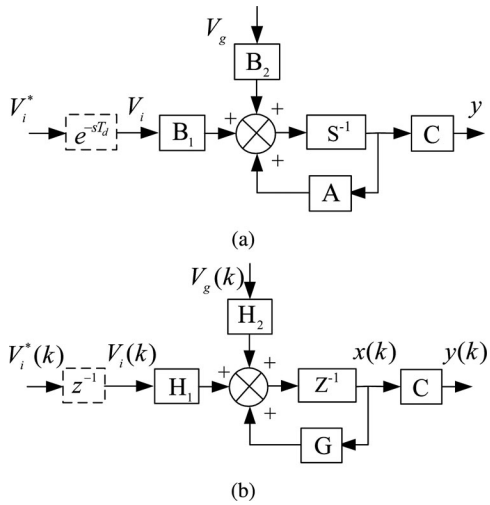

Fig. 2. State-space model of a single-phase grid-connected inverter with *LCL* filter. (a) In continuous domain. (b) In discrete domain.

current law as

$$\dot{x} = Ax + Bu$$
$$y = Cx \tag{1}$$

where

$$A = \begin{bmatrix} -\dfrac{R_1}{L_1} & -\dfrac{1}{L_1} & 0 \\ \dfrac{1}{C_f} & 0 & -\dfrac{1}{C_f} \\ 0 & \dfrac{1}{L_2} & -\dfrac{R_2}{L_2} \end{bmatrix},$$

$$B = \begin{bmatrix} B_1 & | & B_2 \end{bmatrix} = \begin{bmatrix} \dfrac{1}{L_1} & 0 \\ 0 & 0 \\ 0 & -\dfrac{1}{L_2} \end{bmatrix}.$$

The inverter output voltage V_i follows its command V_i^* through a system delay T_d (sum of one sample delay T and PWM transport delay $0.5T$), giving

$$V_i = V_i^* e^{-sT_d}. \tag{2}$$

The continuous generalized control plant derived from (1) and (2) is presented in Fig. 2(a).

B. Modeling in z-Plane

Due to small sampling interval T, the grid voltage V_g can be considered constant in each interval. Thus, the system state-space equation can be obtained by means of zero-order hold as

$$x(k+1) = Gx(k) + Hu(k)$$
$$y(k) = Cx(k) \tag{3}$$

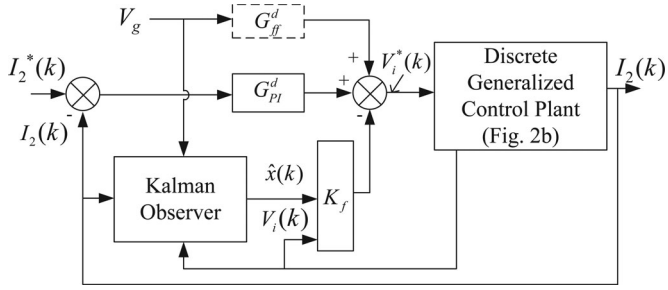

Fig. 3. Control block diagram for discrete state feedback.

where

$$G = e^{AT} = \mathcal{L}^{-1}\left[(sI - A)^{-1}\right]$$
$$H = \begin{bmatrix} H_1 & | & H_2 \end{bmatrix} = \int_0^T G(t)dtB.$$

Here, $\mathcal{L}^{-1}$ is the inverse Laplace transform. The symbolic matrixes are presented in Appendix A.

Similarly, the inverter input voltage and its command in z-domain are governed by the following equation:

$$V_i^*(k) = V_i(k+1). \tag{4}$$

Taken V_i as another state variable [13], the whole system can be modeled as (5) and the corresponding plant is presented in Fig. 2(b)

$$\begin{bmatrix} x(k+1) \\ V_i(k+1) \end{bmatrix} = \begin{bmatrix} G & H_1 \\ 0|_{1\times 3} & 0 \end{bmatrix} \begin{bmatrix} x(k) \\ V_i(k) \end{bmatrix} + \begin{bmatrix} 0|_{3\times 1} \\ 1 \end{bmatrix} V_i^*(k) + \begin{bmatrix} H_2 \\ 0 \end{bmatrix} V_g(k). \tag{5}$$

C. Discrete State Feedback Control

The expanded state vector is defined as $x' = \begin{bmatrix} x & V_i \end{bmatrix}^T$. As depicted in Fig. 3, all the states are feedback through the vector $K_f = \begin{bmatrix} K_{I_1} & K_{V_{C_f}} & K_{I_2} & K_{V_i} \end{bmatrix}$. A Kalman observer is employed to reduce sensors required, while $\hat{x}$ is the estimated state vector. Here, G_{PI}^d is the discrete PI controller expressed by $K_P + K_I/(1 - z^{-1})$, and G_{ff}^d is the discretized GVFF path to be addressed in the next section. Taking into account the orders introduced by one sample delay as well as PI controller, the system is clearly of fifth-order.

Pole placement can be accomplished either by *linear quadratic regulate* or by *direct pole placement*. Since system performance is highly dependent on the poles, the direct one, which is straightforwardly oriented to the final behavior, is preferred in this paper, while the relative issues have been tackled in the author's previous work [22].

The remainder of this paper is dedicated to the GVFF strategy design. A flowchart of the GVFF design procedure is illustrated in Fig. 4, where the numbers indicate the design order. The derivation of discrete plant is achieved by Phases 1–3, while the following steps are focusing on mapping the discrete controlled system into the continuous domain to obtain the GVFF path. It is worth mentioning that although directly acquiring the GVFF

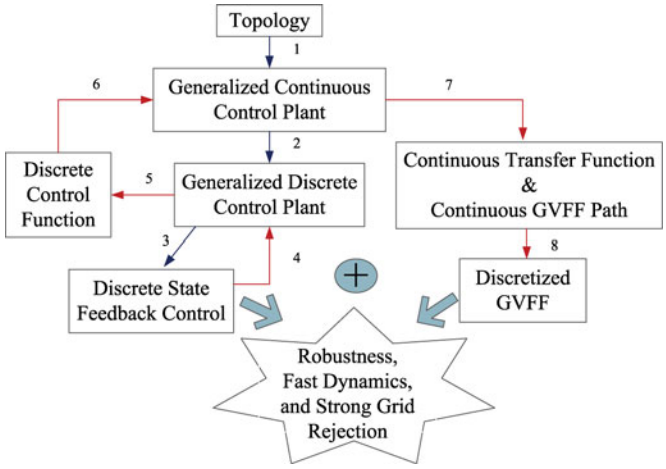

Fig. 4. Developing GVFF for discrete state feedback controller.

path based on the continuous state feedback controller might serves as a simple way, it unavoidably suffers from stability problem and is unfeasible for practical application, which will be addressed in the following section.

III. Proposed Continuous Transformation and Full GVFF Path

The grid voltage, usually rich of various harmonics, is such a mass disturbance on the inverter that seriously distorts the grid current if not suppressed effectively. The inverter output impedance is defined to describe the grid rejection capability as

$$R_o(s)=\frac{V_g(s)}{I_2(s)}=\frac{D(s)}{F(s)} \text{ or } R_o(z)=\frac{V_g(z)}{I_2(z)}=\frac{D(z)}{F(z)} \quad (6)$$

where $D(s)/D(z)$ is the characteristic polynomial determined by the main loop of system, while $F(s)/F(z)$ is the disturbance path.

The larger the impedance, the stronger the grid-voltage rejection capability. The output impedance can be significantly improved either by maximizing the gain of $D(s)/D(z)$ at frequencies concerned or by minimizing the gain of $F(s)/F(z)$. The function of full GVFF addressed here is dedicated to reducing the gain of $F(s)$. Considering the high complexity in z-plane, a continuous transformation is expected to facilitate the establishment of the full GVFF path.

A. Continuous Transformation and Full GVFF Path

In most of reference paper, the GVFF path is obtained in the continuous domain, while it is discretized and implemented in the digital controller to pursue the performance achieved in the continuous domain. Similarly, the discrete system can be transformed to a continuous one to derive the full GVFF path. Referring to Fig. 3, the inverter voltage command can be obtained

$$V_i^*(k)=G_{PI}^d[I_2^*(k)-I_2(k)]-K_f x'(k)+G_{ff}^d V_g(k). \quad (7)$$

This is the so-called discrete control function in Phase 5 in Fig. 4. By mapping it into the generalized continuous control plant shown in Fig. 2(a), we obtain

$$V_i^*=G_{\mathrm{PI}}^s(I_2^*-I_2)-K_f x'+G_{ff}^s V_g \quad (8)$$

where $G_{\mathrm{PI}}^s=K_P+K_i/s, K_i=K_I/T$, G_{ff}^s is the continuous counterpart of G_{ff}^d, and the continuous indicator (s) has been omitted for simplicity. Noting K_f' the feedback gain vector of the original state variables, i.e., $K_f'=[\,K_{I_1}\quad K_{V_{C_f}}\quad K_{I_2}\,]$, substituting (2) into (8) results in

$$V_i=\frac{G_{PI}^s(I_2^*-I_2)-K_f' x+G_{ff}^s V_g}{e^{sT_d}+K_{V_i}}. \quad (9)$$

Notice the difference between $K_f x'$ and $K_f' x$, as the former one is the expanded state feedback, while the latter one is the original state feedback. Equation (9) is then substituted into (1) and the whole continuous closed-loop transfer function can be obtained as

$$\begin{aligned} I_2&=\frac{C\{B_1G_{\mathrm{PI}}^s I_2^*+[B_2(e^{sT_d}+K_{V_i})+B_1G_{ff}^s]V_g\}}{(sI-A)(e^{sT_d}+K_{V_i})+B_1(G_{\mathrm{PI}}^s C+K_f')}\\ &=\frac{1}{D}\{(K_P s+K_i)I_2^*-[C_f L_1(K_{V_i}+e^{sT_d})s^2\\ &\quad+C_f K_{I_1}s+(K_{V_{C_f}}+K_{V_i}+e^{sT_d})-G_{ff}^s]sV_g\} \end{aligned} \quad (10)$$

where I is the identity matrix and D is the characteristic polynomial

$$\begin{aligned} D&=C_f L_1 L_2(K_{V_i}+e^{sT_d})s^4+C_f K_{I_1}L_2 s^3\\ &\quad+[(L_1+L_2)(e^{sT_d}+K_{V_i})+K_{V_{C_f}}L_2]s^2\\ &\quad+(K_{I_1}+K_{I_2}+K_P)s+K_i. \end{aligned}$$

Hence, the GVFF path can be derived by equating the second term of the left side of (10) to zero

$$\begin{aligned} G_{ff}^s&=C_f L_1(K_{V_i}+e^{sT_d})s^2+C_f K_{I_1}s\\ &\quad+(K_{V_{C_f}}+K_{V_i}+e^{sT_d}) \end{aligned} \quad (11)$$

and its alternate form by first-order Taylor expanding as

$$\begin{aligned} G_{ff}^s=&C_f L_1 T_d s^3+C_f L_1(1+K_{V_i})s^2\\ &+(T_d+C_f K_{I_1})s+K_{V_{C_f}}+K_{V_i}+1 \end{aligned} \quad (12)$$

where the coefficients are clear as long as the discrete state feedback controller has been set.

B. Verification

All numerical evaluations hereinafter are based on the parameters listed in Table I. The direct pole placement controller is designed. Subsequently, the comparison of the system before and after transformation is comprehensively investigated in terms of open-loop frequency response, step response, and output impedance to evaluate the validity of the proposed GVFF strategy.

The poles are specified following the guideline presented in [22]

$$p_{2,3}=e^{(-\zeta\pm j\sqrt{1-\zeta^2})\omega_n T}$$

TABLE I
SETUP PARAMETERS

Symbol	Quantity	Value
P_o	Rated Power	1 kW
V_{dc}	Dc Bus	378 V
V_g	Grid Voltage	220 Vrms
f_g	Grid Frequency	50 Hz
L_1	Inverter-side Inductor	1 mH
L_2	Grid-side Inductor	1 mH
C_f	AC Filter Capacitor	4.4 μF
f_c	Switching Frequency	10 kHz
f_s	Sampling Frequency	20 kHz

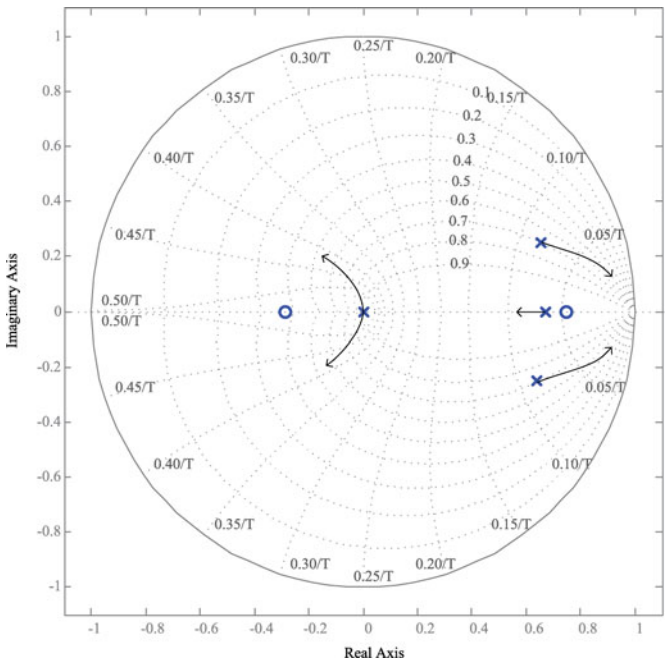

Fig. 5. Discrete pole-zero map with grid impedance varying (frequency unit: Hz). $L_g : 0 \longrightarrow 2.5$mH. Other zeros lying in the negative real axes outside the unit circle are not provided.

$$z_1 = 1 - 0.15\sqrt{\frac{2\pi}{\omega_n T}}[1 - \text{real}(p_2)]$$
$$p_1 = 0.9z_1, p_4 = p_5 = 0 \tag{13}$$

where the damping ratio ζ is usually set as 0.707, and the angular natural resonance frequency ω_n is set as $\min(0.5\omega_r, 0.1 \cdot 2\pi f_s)$; hence, ω_r is the angular filter resonance frequency. The resulting pole-zero map is shown in Fig. 5 and the scaled control parameters are

$$[\,K_P \quad K_I\,] = [\,8.8197 \quad 2.0220\,]$$
$$K_f = [\,13.7919 \quad -1.2618 \quad -7.5489 \quad 0.9594\,].$$

The continuous closed-loop transfer function containing e^{sT_d} here is not numerically convergent; however, the step response is still unveiled thanks to the Taylor' expanding form. Fig. 6 demonstrates the accordance between the discrete performance and its continuous counterpart below the high-frequency region, i.e., lower than 1/5f_s, verifying the validity of continuous transformation. It is worth mentioning that a similar verification for another continuous modeling method using *Pade* approximation for e^{sT_d} has also been performed in [23].

For a continuous system, an infinite output impedance is theoretically possible providing that the GVFF path of (11) can be ideally achieved. However, it is not practical for digital implementation. Considering that the noninteger sample of e^{sT_d} is difficult to realize, the Taylor expansion is employed hereinafter. Without losing generality, the differentiators are discretized by pure backward difference, i.e., $s \rightarrow (1 - z^{-1})/T$. The resulting discrete output impedance is depicted in Fig. 7, where one can see the proportional part of GVFF improves R_o mainly in the low- and medium-frequency range (comparing lines 2 and 3); the first-order part boosts R_o further, at the cost of smaller R_o in the high-frequency range (comparing lines 3 and 4); the second-order part acts in a similar way of the first-order one (comparing lines 4 and 5); however, the third-order part contributes almost nothing but even smaller R_o at high frequency (comparing lines 5 and 1). For this reason, the third-order part is abandoned, otherwise the stability degrades significantly. As a result, the final output impedance R_o is depicted as line 5.

C. Evaluation of Continuous and Discrete State Feedback

Although the state feedback controller can be designed in the continuous domain, there is remarkable discrepancy between these two design approaches. The resulted continuous pole-zero map with Taylor expanding is shown in Fig. 8, with the poles evaluated as

$$s = \{\, 25416 \quad -3241 \pm j17300 \quad -3644 \pm j3173\,\}.$$

It is noticed that none of these poles are mapping with their discrete counterparts through e^{sT}, so is the PI zero. A deep insight shows that the continuous complex poles feature $\omega_n = 4832$ rad/s, $\zeta = 0.754$ and $\omega_n = 17953$ rad/s, $\zeta = 0.184$, respectively, comparing with $\omega_n = 10660$ rad/s, $\zeta = 0.707$ and $\omega_n = \infty, \zeta = 1$ for the discrete ones. Besides, the intrinsic zeros, which are dependent on the sampling frequency, have disappeared in the continuous pole-zero map. In other words, the continuous design is blind to these zeros such that it may lead to problems, especially when inverter current is controlled, for such case features the intrinsic zeros lying on the unit circle within the low frequency region hence requiring to be damped with poles [15]. From a practical point of view, the discrete state feedback should be adopted as benchmark, as it is well accordance with the nature of digital control such that promising performance as expected. On the other hand, the discrepancy manifested previously totally ambiguities the guideline for continuous pole placement, hence makes it unfeasible. Unfortunately, a persuasive explanation for such phenomena has not been available yet. However, with respect to GVFF, it is emphasized that the continuous transformation as well as the full GVFF path is still valid.

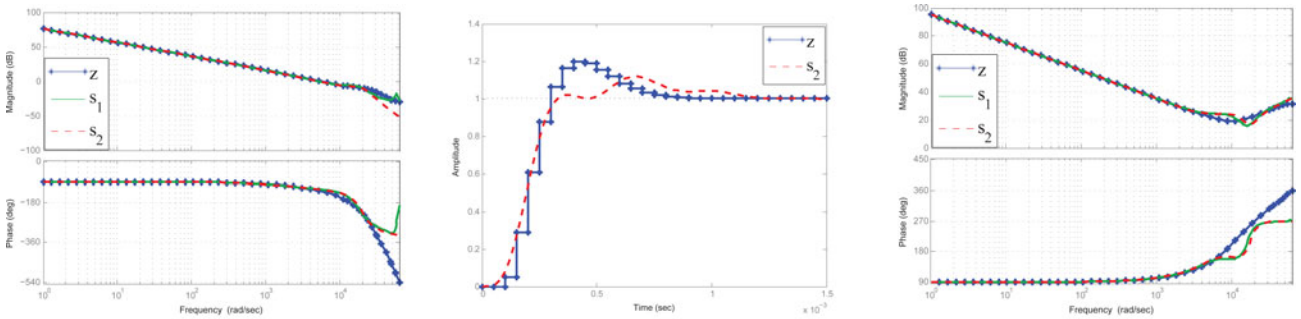

Fig. 6. Comparison between discrete performance and its continuous counterpart. (a) Open-loop frequency response. (b) Step response. (c) Output impedance without GVFF. z–discrete one; s_1–continuous one with e^{sT_d}; s_2–continuous one with Taylor expanding.

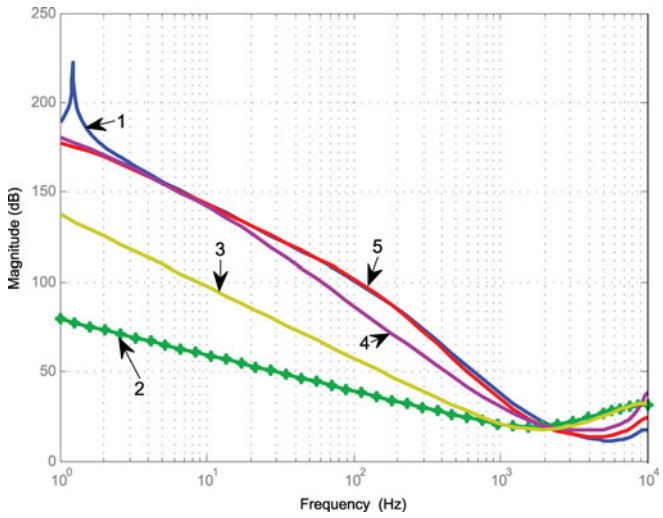

Fig. 7. Output impedance with full GVFF in discrete domain. 1: R_o under full GVFF; 2: R_o under no GVFF; 3: R_o under proportional part of GVFF; 4: R_o under proportional and first-order parts of GVFF; 5: R_o under proportional, first-order and second-order parts of GVFF.

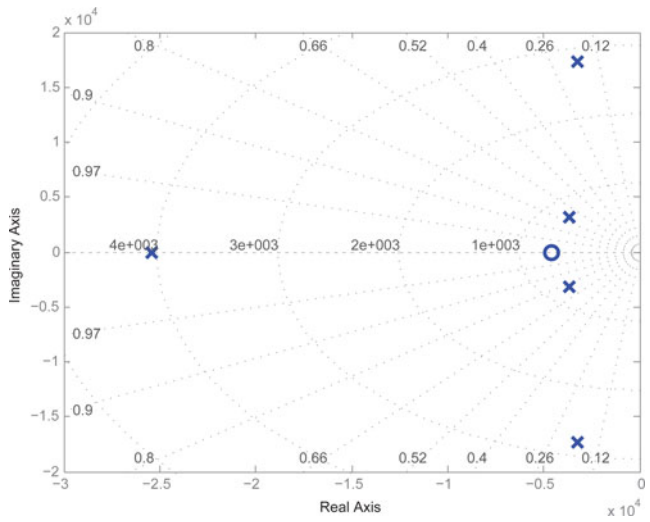

Fig. 8. Continuous pole-zero map of system with discrete state feedback control (frequency unit: Hz).

IV. Stability Analysis and the Proposed Robust Implementation for Full GVFF

Referring to (12), the GVFF path contains multiordered differentiators that exhibit a significant challenge in the feedforward path design, especially for the cases of weak grid and heavy noise. This section is dedicated to addressing this issue.

A. Stability Analysis With GVFF

It can be concluded from (12) that the full GVFF path is independent of PI controller, grid current feedback gain, and the grid-side inductor. This means that the grid impedance has no influence on the full GVFF path, which is of particular concern. However, the grid impedance does jeopardize the effectiveness, through the other part of GVFF—grid voltage sensed at the common coupling point (PCC). Noting $G_{ff}^{s\prime}$ the practiced GVFF path, (10) can be reformulated by replacing V_g with $(L_g s + R_g)I_2 + V_s$, as detailed in Fig. 1

$$I_2 = \frac{G_{PI}^s I_2^* + (-G_{ff}^s + G_{ff}^{s\prime})V_s}{D/s + (G_{ff}^s - G_{ff}^{s\prime})(L_g s + R_g)}. \tag{14}$$

Unless $G_{ff}^s = G_{ff}^{s\prime}$, which would not happen in practical, or the sensitive information of I_2 induced and magnified by the grid impedance will inevitably flow into the main loop, hence alter the stability.

Equation (14) is continuous and only serves to qualitative analysis. The following case studies are carried out in the discrete domain, using pole-zero maps, to determine the grid compatibility of such inverter. First, pure differentiator is employed as benchmark. Because this case is highly susceptible to noise, an LPF with expression of $1/(\tau s + 1)$ is employed for each order of differentiator. Without loss of generality, τ is selected as 1 μs; hence, the modified differentiator is discretized by means of zero-pole matched.

The resulting pole trajectories are shown in Fig. 9. It is seen that the system turns to be seventh-order due to the GVFF. When differentiator is purely realized, grid impedance of less than 0.8 mH is in tolerance (as indicated by the bold line). However, such compatibility region is considerably enlarged once the LPF is introduced (as indicated by the dash line). It can be concluded from abundant investigation that the compatibility of grid impedance follows such a way: the more accuracy of

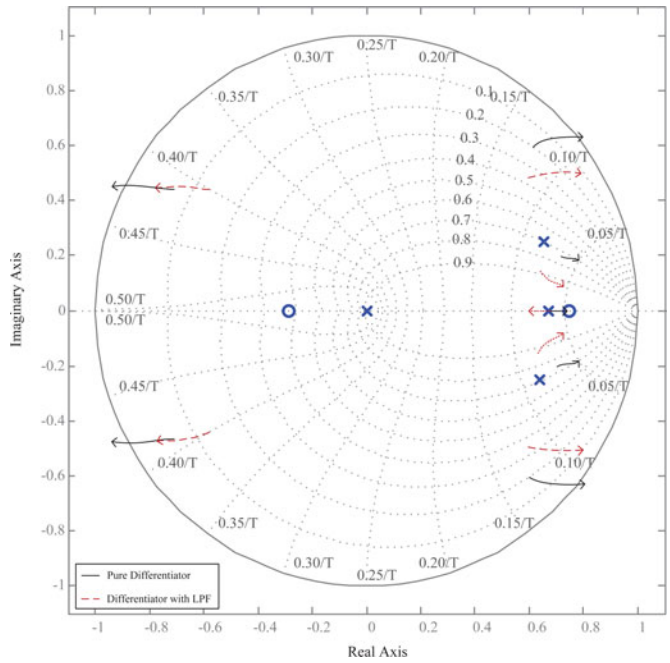

Fig. 9. Poles vary with the grid impedance, when full GVFF is applied (frequency unit: Hz). The trajectory of zeros are not provided for clarity. L_g:0 ⟶ 0.8 mH.

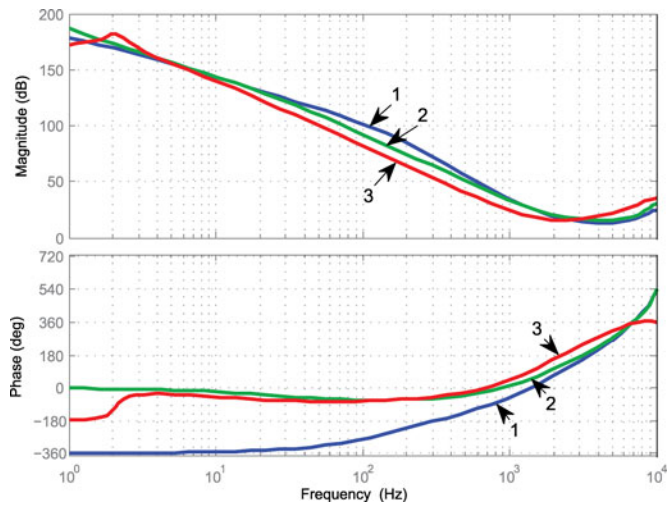

Fig. 10. Output impedance with LPF in discrete domain. 1—$\tau = 0\,\mu$s, 2—$\tau = 10\,\mu$s, 3—$\tau = 100\,\mu$s.

differentiator, the higher requirement for grid-voltage sensing, i.e., either noise or sensing delay should be as small as possible. Of course, such compromise is almost impossible in practice. Otherwise, less accuracy results in more compatibility of grid impedance, however, at the expense of output impedance, as depicted in Fig. 10 (the output impedance is still defined as $V_g(z)/I_2(z)$, regardless of L_g as well as V_s). Moreover, as the grid impedance is usually unknown, the cutoff frequency of LPF should be set low enough. In a word, the obstacle lies in the coordination of accuracy and robustness.

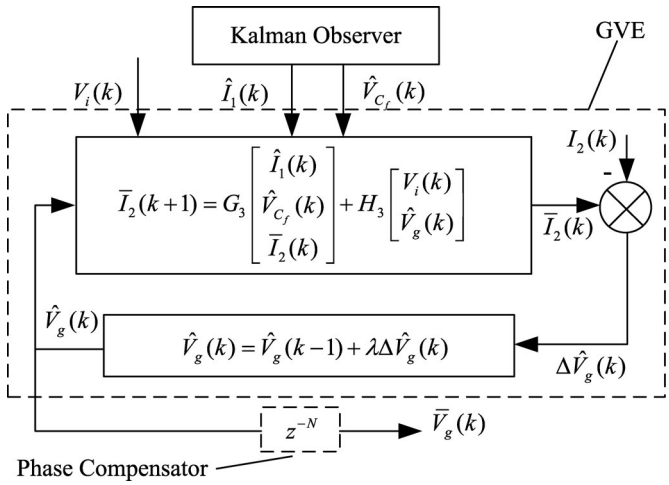

Fig. 11. GVE with phase compensator (z^{-N}). G_3 and H_3 are the third-row elements in matrixes G and H, respectively.

B. Proposed Robust Implementation for Full GVFF

It is so challenging to design an accurate but noise-immune differentiator that the sensed grid voltage is not suitable for GVFF any longer. A "clean" grid voltage can then be restored for substitution. Bolsens *et al.* [14] employ another Kalman observer to estimate the grid voltage. However, the computational burden increases sharply with the harmonics concerned. Then, the GVE employed for sensorless operation [21], [24] is more popular, for it is able to inherently capture a grid voltage that highly resembles the actual one but noiseless. The schematic is shown in Fig. 11, manifesting itself built up by the integration of error between actual grid current and its estimated evolution using the grid-voltage estimation. Since the Kalman observer for states has been developed (see Fig. 3), the increased complexity is fixed and low.

However, unlike the sensorless operation, the grid-voltage transducer is still kept for grid synchronization as well as for state rebuilding by Kalman observer. Although the voltage transducer introduces additional cost, the system robustness can be guaranteed, either in scenario of islanding detection, or in the startup phase, which otherwise features overshoot current occurring due to the convergence time of voltage estimation [24]. A selection rule of the integral gain is presented in [21], expressed as $\lambda < 2L_1(L_1 + L_2)/T^2$. However, one should keep the gain small enough to avoid deteriorating the whole stability, though conditioned by the accuracy of estimate grid voltage.

An extra procedure of z^{-N}, namely phase compensator, is proposed to eliminate the phase error between the estimated grid voltage and the actual one. Such phase error results from the finite gain of the integer (λ), in a similar fashion as closed-loop control with PI controller tracks the sinus reference but results in nonzero steady error. On the other hand, z^{-N} is to obtain advance phase by delaying the estimated grid voltage by less than one cycle, as the grid voltage evolves periodically. Moreover, the one-cycle-delay characteristic also avoids ringing that may be induced by the feedforward path during dynamic operation. Thus, such a GVE can be interpreted as an expanded Kalman

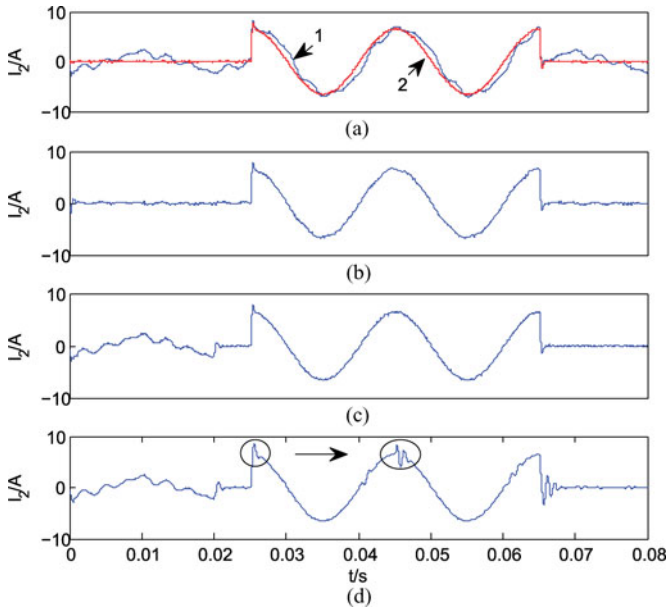

Fig. 12. Simulation grid current under stiff/weak grid. (a) Stiff grid assumed. 1—without GVFF, 2—with sensed grid voltage plus pure differentiator for GVFF. (b) Stiff grid assumed. Estimate grid voltage without phase compensation for full GVFF. (c) Stiff grid assumed. Estimate grid voltage with phase compensation for full GVFF. (d) Weak grid assumed, where the grid impedance is the same as grid inductor. Estimate grid voltage with phase compensation for full GVFF. The marked exhibits the inertial effect of phase compensator.

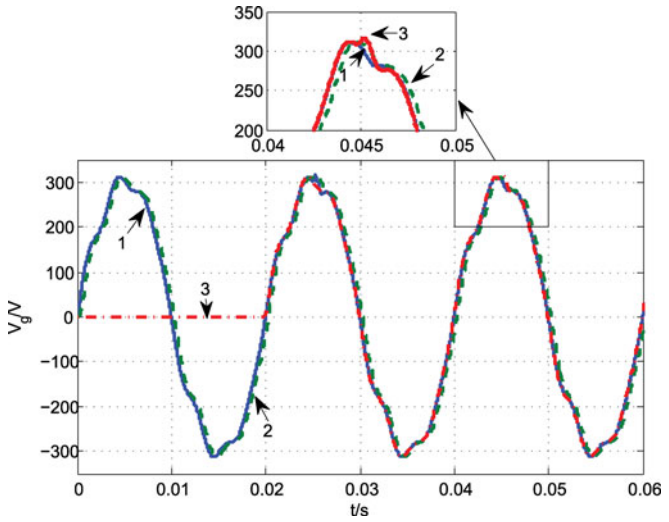

Fig. 13. Simulation result of GVE with phase compensator. Weak grid assumed ($L_g = L_2$, $R_g = R_2$). 1—the actual grid voltage; 2—the output of GVE without phase compensator; 3—the output of GVE with phase compensator. The zoomed distort of GVE is transferred from the pass grid cycle at the trigger moment by the phase compensator.

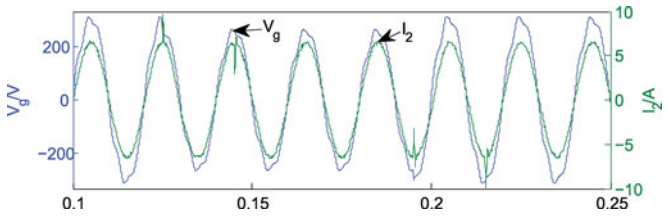

Fig. 14. Simulation result under grid swag mode.

filter for the grid voltage, except for requiring the inverter model rather than the grid-voltage model.

V. Simulation Results

A MATLAB/Simulink model is developed for simulation where the solver is chosen as variable step discrete with step of 0.2 μs. The inverter parameters listed in Table I are employed for both simulation and experiments. In order to test the grid-voltage rejection capability, the third, fifth, and seventh harmonics with content of 4.82%, 4.18%, and 3.54%, respectively, are introduced in the grid voltage. The dynamic performance is tested by switching the load from empty to rated value at the peak and vice versa.

The simulation results under stiff/weak grid are shown in Fig. 12, without current-track-error limiter inserted in the signal path. Fig. 12(a)–(c) assumes stiff grid impedance. The comparison between the current waveforms shown in Fig. 12(a) further verifies the validity of GVFF path established previously. The comparison of current waveforms shown in Fig. 12(b) and (c), respectively, necessities the phase compensator. The current waveform in Fig. 12(d), where weak grid is assumed, i.e., grid impedance is the same as grid inductor, demonstrates that the system is robust to the variation of grid impedance, though with somewhat disorder during startup (lasts for near one cycle), resulting from the initiation of phase compensator in GVE, as illustrated in Fig. 13. If necessary, such disorder can be removed in the initial current cycle, either by using the sensed grid voltage for the proportional part of GVFF, or by using GVE output before the phase compensator. Besides, the distortion in the grid voltage at the trigger moment would transfer to the next current cycle, as marked in Fig. 12(d). This results from the one-cycle-delay characteristic of the phase compensator, hence can be recognized as inertia, while a zoomed view can also be found in Fig. 13. Notice that an improperly high integral gain of GVE as well as high grid impedance would enhance this efficacy. However, with proper integral gain and moderate rate of current reference, it should normally not be troublesome, even in weak grid.

The proposed strategy is also tested with step change of the grid voltage. When it is suddenly decreased by 15% and then recovered after 3.5 line cycles, the waveforms are shown in Fig. 14. It can be seen that the grid current responds to the voltage variation quickly in an inverse direction and gets to the steady state within 3 line cycles. Due to the inertia of GVE through GVFF, the grid current exhibits one more current spikes after the step change of the grid voltage.

A local *RLC* load with quality factor of 2.5 and resonant frequency of 50 Hz is chosen to test the islanding behavior of the proposed strategy. When the grid voltage is disconnected at 1.4 s, the PCC voltage, frequency, and the output current waveforms are shown in Fig. 15, where the current I_2 is scaled by a factor of 30 to make it visible. As shown in Fig. 15(a), due the close match of the local load and the inverter output active power, the amplitude of the PCC voltage varies little. In

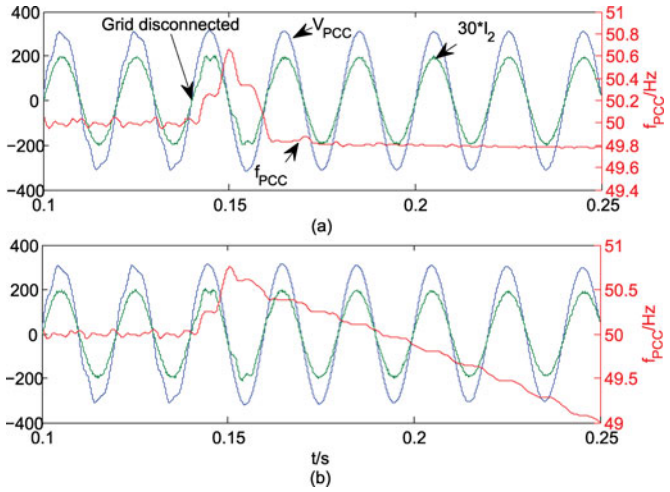

Fig. 15. Simulation results under islanding detection mode. V_{PCC} and I_2 are presented in volts and amperes, respectively. (a) Without active islanding method. (b) With active islanding method (APS).

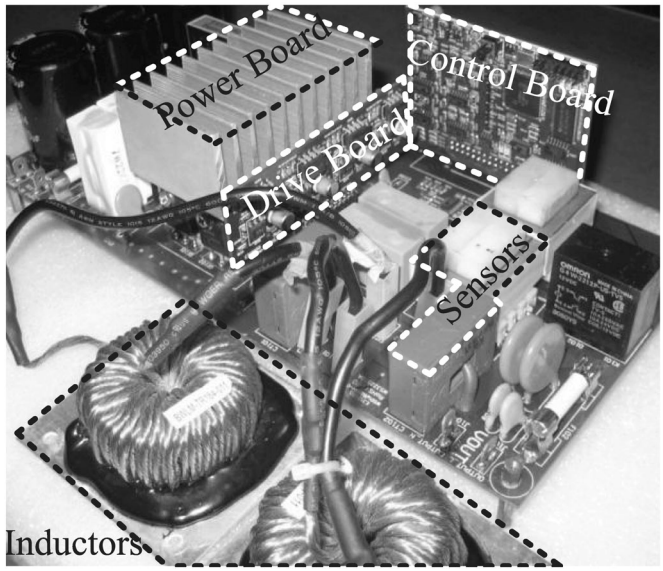

Fig. 16. Single phase grid-connected inverter prototype.

addition, the PCC frequency can still be seen within the range of 49.5–50.5 Hz. Notice that the frequency spike is the transient response of the PLL to the change of PCC voltage. This means that the outage of the utility may not be identified so that active islanding detection strategies are still required, e.g., auto phase shift (APS) [25], by which islanding is successfully detected within about 4 line cycles, as shown in Fig. 15(b). Thus, it exhibits that with the proposed control strategy, active islanding is still necessary to ensure the safety operation of the inverter.

VI. Experimental Results

A 1-kW prototype is built to verify the proposed method, as shown in Fig. 16. The dc bus is formed by a dc source. The control chip is 32-bit fixed-point 100-MHz TMS320F2808. With the help of Kalman observer, only the grid current, the grid voltage, and the dc bus are sensed. An isolated 3-kVA 1:1 transformer is connected between the grid and PCC to emulate the practical environment, with parasitic parameters left undetected.

The control schematic is shown in Figs. 3 and 11. The sample action is taken at the top and bottom of the carrier signal. Current reference generation as well as grid synchronization is realized by filtering the modulus-scaled sampled grid voltage with an ABPF. The measurement noise of grid current is set to 50 mA (monitored). The process noise in terms of inverter voltage (contributed by process noise, etc.) and grid voltage are set to be 0.5 V (estimate) and 3.5 V (monitored), respectively. Finally, the feedback vector of Kalman observer is numerically obtained using MATLAB. The Kalman observer, GVE, full GVFF, and state feedback are realized by a small set of C code arrays and the total computing time of the proposed current controller is about 6 μs, comparing with the interrupt interval of 50 μs. Besides, a current-track-error limiter is inserted in the signal path to obtain a limitation to 1.5 A.

A. Steady Operation Under Normal Grid

Normal grid is assumed first, i.e., the grid impedance is represented by the transformer impedance only.

Fig. 17(a) shows the results in case of GVFF with LPF, which is discretized by the mean of pole-zero matched. However, the result without any feedforward of grid voltage is not provided, since the inverter is triggered by the overcurrent once PWM is activated, due to the small startup impedance. The comparison among grid current waveforms as well as the corresponding total harmonic distortion (THD) shown in Fig. 17(b) demonstrates the necessity of full GVFF. Although the smaller τ of LPF, the stronger grid rejection, the current waveform 4 demonstrates that the stability will be weaker, where extra current distortion as marked, together with audible noise, is induced by applying LPF with $\tau = 20\,\mu$s instead of $\tau = 50\,\mu$s, though the grid current THD is reduced. So, it is hard to coordinate the accuracy and robustness with LPF for GVFF.

The result in the case of PR+HC controller instead of PI controller is also provided in Fig. 18(a). The PR+HC controller is expressed as

$$G_{\mathrm{PR+HC}}(s) = K_P + K_i \frac{2\zeta'\omega_g s}{s^2 + 2\zeta'\omega_g s + {\omega_g}^2} + \frac{K_i}{3} \sum_{n=3,5,7} \frac{2\zeta' n\omega_g s}{s^2 + 2\zeta' n\omega_g s + (n\omega_g)^2} \quad (15)$$

where the gain is the same with the PI controller; hence, ζ' is the damping factor of the quadratic generalized integer, which is set 0.025 here. The current waveform together with its THD shown in Fig. 18(b) demonstrates the necessity of harmonic compensators with order up to eleventh. However, as stated in [26], the higher the order, the smaller the phase margin. Besides, the increasing computational burden also remains an issue, for each harmonic compensator takes 1.6μs to run.

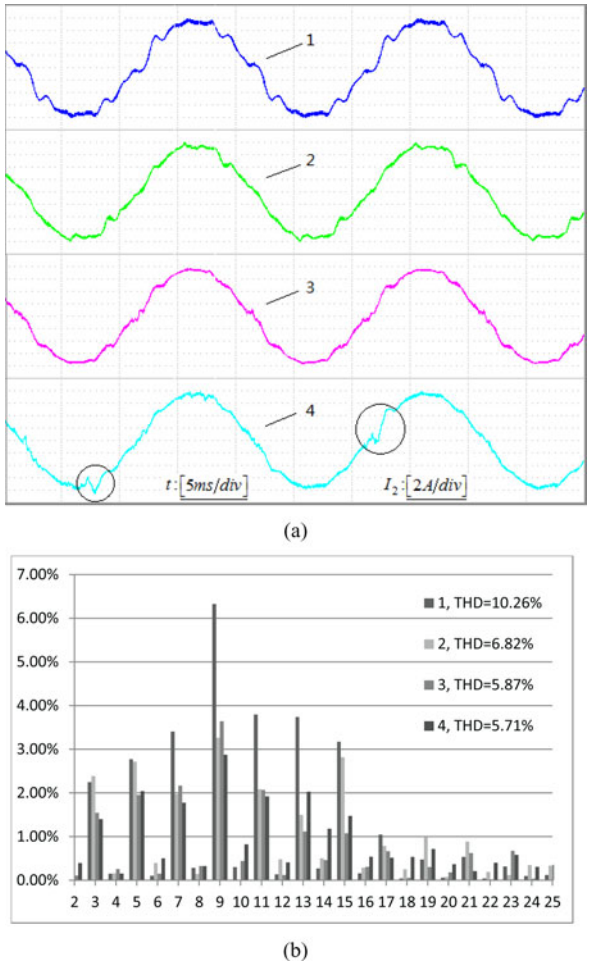

Fig. 17. Experimental grid current waveform of steady operation, using LPF for GVFF, normal grid assumed 1—with proportional component of GVFF, $\tau = 50\,\mu$s; 2—with proportional and first-order components of GVFF, $\tau = 50\,\mu$s; 3—with full GVFF, $\tau = 50\,\mu$s; 4—with full GVFF, $\tau = 20\,\mu$s. (a) Grid current waveform. (b) Grid current harmonic magnitude percent of the rated fundamental amplitude.

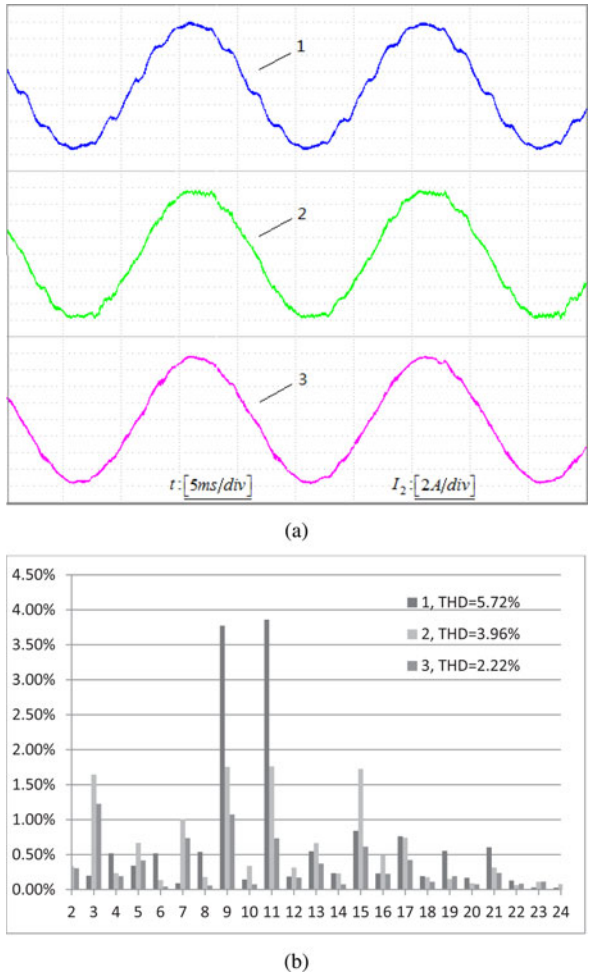

Fig. 18. Experimental grid current waveform of steady operation, normal grid assumed. 1—PR+HC; 2—full GVFF using GVE without phase compensator; 3—full GVFF using GVE with phase compensator.

In contrast, the results in case of full GVFF with GVE are presented in Fig. 18(a). It clearly manifests the high performance offered by full GVFF with GVE; hence, the phase compensator serves to improve the power quality further, as indicated by Fig. 18(b). Specifically, the phase compensator functions not only to make the estimate grid voltage coincident with the actual one, but also to compensate the deviation between the estimate states and the actual states, by providing more lead phase. In this paper, λ and N are set as 2.5 and 393, respectively; hence, the time constant of analogous LPF used for sampling grid voltage is set as 12 μs.

B. Dynamic Operation Under Normal Grid

Then, still under normal grid, Fig. 19(a) shows the dynamic result in case of full GVFF with LPF ($\tau = 50\,\mu$s), which features smooth and rapid transient response. In contrast, the transient response in case of PR+HC controller is much dependent on the damping factor ζ', i.e., the bigger the ζ', the faster the response. However, in order to get a low bandwidth so that the selective harmonic compensation be effective, ζ' should not be too big [26]. On the other hand, in the case of full GVFF with GVE (with phase compensator), there is current spike as shown in Fig. 19(c), which is in accordance with the simulation results, as caused by the inertia of the phase compensator. Such spike fades with time under the condition that either the current-reference rate or the grid impedance is moderate. This means that the previous grid-voltage spike induced by the previous current change is not able to produce an equivalent current spike, so that the impact on the PCC voltage is not as strong as the previous one. With this interactivity going on, there comes no spike eventually.

C. Dynamic Operation Under Weak Grid

Next, to testify the robustness against the grid impedance variation, weak grid is emulated by inserting another inductor same as L_2 between the inverter output and the transformer. The result in case of full GVFF with LPF ($\tau = 50\,\mu$s) is shown in Fig. 20(a), which is almost identical with that under normal grid [referring Fig. 19(a)]. It happens similarly in case of PR+HC controller, as shown in Fig. 20(b). However, in case of GVFF

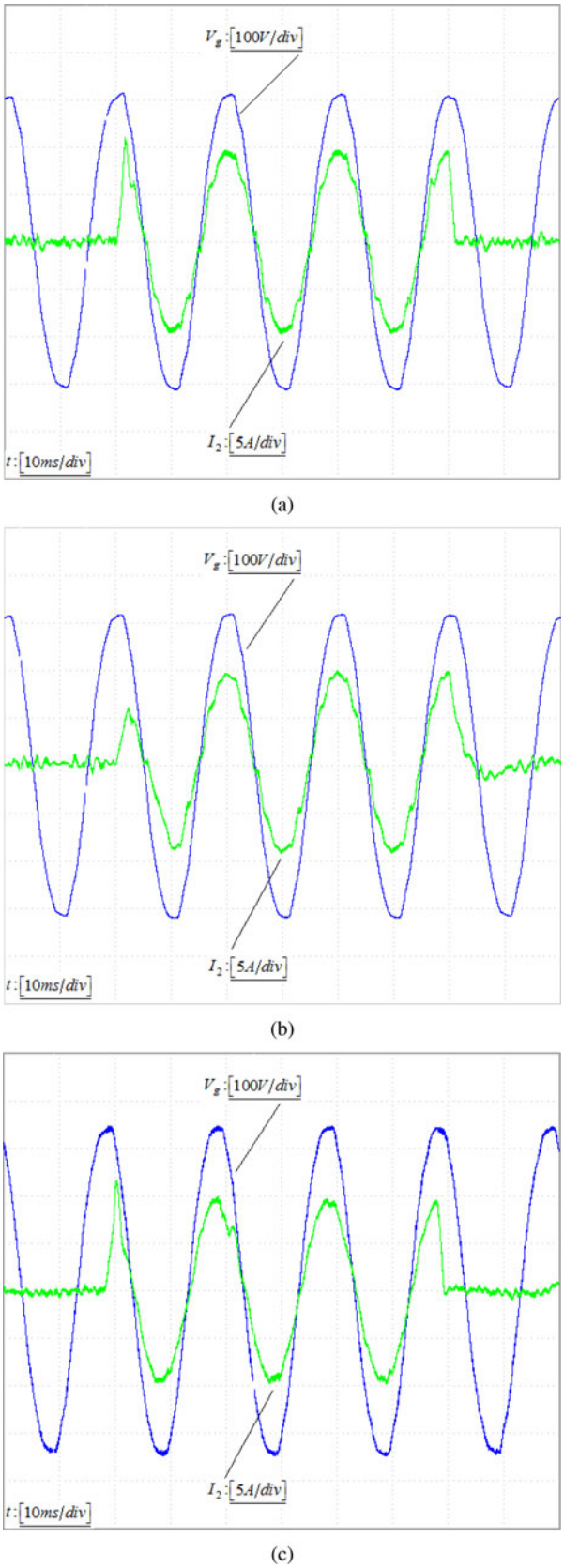

Fig. 19. Experimental result of empty/rated load switch. Normal grid assumed. (a) Full GVFF with LPF ($\tau = 50\,\mu$s). (b) PR+HC controller. (c) Full GVFF with GVE (with phase compensator).

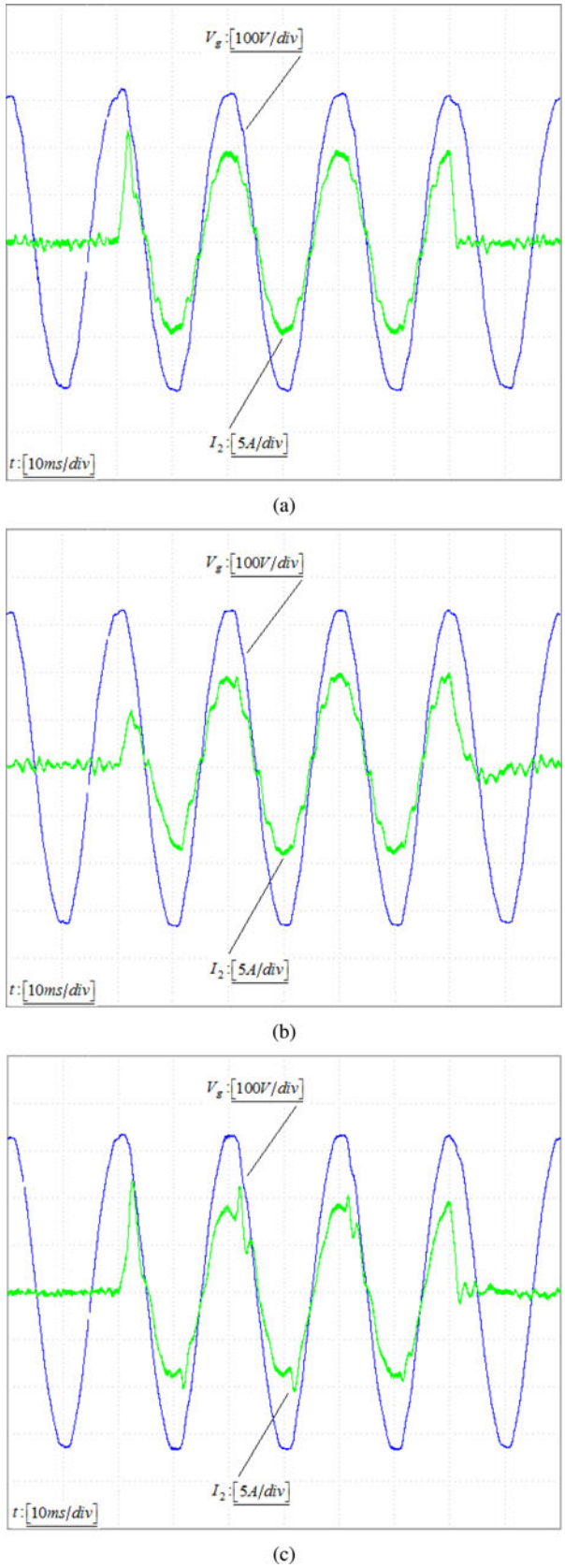

Fig. 20. Experimental result of empty/rated load switch. Weak grid assumed. (a) Full GVFF with LPF ($\tau = 50\,\mu$s). (b) PR+HC controller. (c) Full GVFF with GVE (with phase compensator).

with GVE (with phase compensator), there is more current distortion, which is again caused by the inertia effect of the phase compensator, hence enhanced by the grid impedance. Notice that the weaker performance of GVE (without phase compensator) under weak grid is also blamed, as reflected by the distortion at the negative current peak. It can thus be concluded that the super steady current waveform offered by full GVFF with GVE is somewhat at the cost of dynamic performance under weak grid, though is still acceptable.

VII. Conclusion

The discrete state feedback control for grid-connected inverter with *LCL* filter offers excellent reference tracking ability, while the coupling of grid voltage and current introduced by the multifeedback makes the voltage feedforward rather difficult. A full feedforward of grid voltage for discrete state feedback controlled grid-connected inverter with *LCL* filter is proposed in this paper by transforming the discrete controlled system into its continuous counterpart to derive the GVFF path. Such path represents an extension to the existing ones. The transformation process and the corresponding theoretical verification are provided as well. Moreover, the robustness analysis of the proposed strategy to the grid impedance is also performed. In the feedforward path, high-order differentiators are required that are sensitive to the grid impedance and the noise. An improved GVE is employed to successfully solve such problems. Therefore, the proposed strategy enables the grid-connected inverter to have super steady waveform, dynamic waveform and robustness to the variation of grid impedance and grid-voltage harmonics, while the complexity remains moderate and the computational burden is low. Simulation and experimental results verified the feasibility and validity of the proposed strategy.

Appendix A

Symbolic Matrixes

Regardless of the parasitic resistances, the discrete state transfer matrix is expressed by

$$G=\begin{bmatrix} \dfrac{L_1+L_2\cos\omega_r T}{L_1+L_2} & -\dfrac{\sin\omega_r T}{\omega_r L_1} & \dfrac{L_2(1-\cos\omega_r T)}{L_1+L_2} \\ \dfrac{\sin\omega_r T}{\omega_r C_f} & \cos\omega_r T & -\dfrac{\sin\omega_r T}{\omega_r C_f} \\ \dfrac{L_1(1-\cos\omega_r T)}{L_1+L_2} & \dfrac{\sin\omega_r T}{\omega_r L_2} & \dfrac{L_2+L_1\cos\omega_r T}{L_1+L_2} \end{bmatrix}$$

and the input matrix is expressed by

$$H=\frac{1}{L_1+L_2}\begin{bmatrix} T+\dfrac{L_2\sin\omega_r T}{\omega_r L_1} & -T+\dfrac{\sin\omega_r T}{\omega_r} \\ L_2(1-\cos\omega_r T) & L_1(1-\cos\omega_r T) \\ T-\dfrac{\sin\omega_r T}{\omega_r} & -T-\dfrac{L_1\sin\omega_r T}{\omega_r L_2} \end{bmatrix}$$

where $\omega_r=\sqrt{\frac{L_1+L_2}{L_1L_2C_f}}$.

Appendix B

Full GVFF Paths for Other Operations

It is also common to utilize the predictive nature of the estimated quantities to compensate for total system delays. The following is dedicated to establishing the corresponding full GVFF path.

In a first step, we obtain the discrete control function

$$V_i(k)=G_{\mathrm{PI}}^d[I_2^*(k)-\hat{I}_2(k)]-K_f\hat{x}(k)+G_{ff}^dV_g(k-1). \tag{16}$$

Here, the feedback gain vector is redefined as $K_f=[\,K_{I_1}\quad K_{V_{C_f}}\quad K_{I_2}\,]$. One should also notice that $V_g(k-1)$ results from the fact that the delay compensation deals with the main loop only, while in the feedforward path, there is still delay.

Then, mapping (16) into continuous domain [see Fig. 2(a)] results in the continuous control function

$$V_i=G_{\mathrm{PI}}^s(I_2^*-I_2)-K_fx+G_{ff}^sV_ge^{-sT_d}. \tag{17}$$

Next, substitution of (17) into (1) results in the whole continuous transfer function as

$$\begin{aligned} I_2&=\frac{C[B_1G_{\mathrm{PI}}^sI_2^*+(B_1G_{ff}^se^{-sT_d}+B_2)V_g]}{sI-A+B_1(G_{\mathrm{PI}}^sC+K_f)} \\ &=\frac{1}{D}\{(K_Ps+K_i)I_2{}^*-(C_fL_1s^2+C_fK_{I_1}s \\ &\quad+K_{V_{C_f}}+1-G_{ff}^se^{-sT_d})sV_g\} \end{aligned} \tag{18}$$

where

$$\begin{aligned} D&=C_fL_1L_2s^4+C_fK_{I_1}L_2s^3+(L_1+L_2+K_{V_{C_f}}L_2)s^2 \\ &\quad+(K_P+K_{I_1}+K_{I_2})s+K_i. \end{aligned}$$

Finally, the full GVFF path is derived from (18) as

$$G_{ff}^s=(C_fL_1s^2+C_fK_{I_1}s+K_{V_{C_f}}+1)e^{sT_d} \tag{19}$$

and its Taylor expanding form as

$$\begin{aligned} G_{ff}^s&=C_fL_1T_ds^3+C_f(L_1+K_{I_1}T_d)s^2 \\ &\quad+[(K_{V_{C_f}}+1)T_d+C_fK_{I_1}]s+K_{V_{C_f}}+1. \end{aligned} \tag{20}$$

It is worthy to point out that (19) is the generalization of the GVFF path presented in [9], which is specific for the case with capacitor current feedback for damping, and e^{sT_d} disregarded, i.e., $K_f=[\,K_{I_1}\quad 0\quad -K_{I_1}\,]$.

For other cases, e.g., inverter current is set as control object, one only needs to alter the output vector C in (1), while the remaining manipulation is almost the same. Moreover, if active damping is filter based [19], the full GVFF path is simplified as (grid current controlled)

$$G_{ff}^s=C_fL_1T_ds^3+C_fL_1s^2+T_ds+1. \tag{21}$$

REFERENCES

[1] F. Blaabjerg, R. Teodorescu, and M. Liserre, "Overview of control and grid synchronization for distributed power generation systems," *IEEE Trans. Ind. Electron.*, vol. 53, no. 5, pp. 1398–1409, Oct. 2006.

[2] M. Liserre, F. Blaabjerg, and S. Hansen, "Design and control of an LCL-filter-based three-phase active rectifier," *IEEE Trans. Ind. Appl.*, vol. 41, no. 5, pp. 1281–1291, Sep./Oct. 2005.

[3] M. Liserre, R. Teodorescu, and F. Blaabjerg, "Stability of photovoltaic and wind turbine grid-connected inverters for a large set of grid impedance values," *IEEE Trans. Power Electron.*, vol. 21, no. 1, pp. 263–272, Jan. 2006.

[4] V. Blasko and V. Kaura, "A novel control to actively damp resonance in input LC filter of a three-phase voltage source converter," *IEEE Trans. Ind. Appl.*, vol. 33, no. 2, pp. 542–550, Mar./Apr. 1997.

[5] M. Malinowski and S. Bernet, "A simple sensorless active damping solution for three phase PWM rectifier with LCL filter," *IEEE Trans. Ind. Electron.*, vol. 55, no. 4, pp. 1876–1880, Apr. 2008.

[6] F. Liu, Y. Zhou, S. Duan, J. Yin, B. Liu, and F. Liu, "Parameter design of a two-current-loop controller used in a grid-connected inverter system with LCL filter," *IEEE Trans. Ind. Electron.*, vol. 56, no. 11, pp. 4483–4491, Nov. 2009.

[7] W. Gullvik, L. Norum, and R. Nilsen, "Active damping of resonance oscillations in LCL-filters based on virtual flux and virtual resistor," in *Proc. Eur. Conf. Power Electron. Appl.*, 2007, pp. 1–10.

[8] E. Twining and D. G. Holmes, "Grid current regulation of a three-phase voltage source inverter with an LCL input filter," *IEEE Trans. Power Electron.*, vol. 18, no. 3, pp. 888–895, May 2003.

[9] X. Wang, X. Ruan, S. Liu, and C. K. Tse, "Full feedforward of grid voltage for grid-connected inverter with LCL filter to suppress current distortion due to grid voltage harmonics," *IEEE Trans. Power Electron.*, vol. 25, no. 12, pp. 3119–3126, Dec. 2010.

[10] G. Shen and D. Xu, "An improved control strategy for grid-connected voltage source inverters with an LCL filter," *IEEE Trans. Power Electron.*, vol. 23, no. 4, pp. 1899–1906, Jul. 2008.

[11] M. Liserre, A. D. Aquila, and F. Blaabjerg, "Genetic algorithm-based design of the active damping for an LCL-filter three-phase active rectifier," *IEEE Trans. Power Electron.*, vol. 19, no. 1, pp. 76–86, Jan. 2004.

[12] J. Dannehl, F. W. Fuchs, S. Hansen, and P. B. Thøgersen, "Investigation of active damping approaches for PI-based current control of grid-connected pulse width modulation converters with LCL filters," *IEEE Trans. Ind. Appl.*, vol. 46, no. 4, pp. 1509–1517, Jul./Aug. 2010.

[13] E. Wu and P. W. Lehn, "Digital current control of a voltage source converter with active damping of LCL resonance," *IEEE Trans. Power Electron.*, vol. 21, no. 5, pp. 1364–1373, Sep. 2006.

[14] B. Bolsens, K. De, J. Van, J. Driesen, and R. Belmans, "Model-based generation of low distortion currents in grid-coupled PWM-inverters using an LCL output filter," *IEEE Trans. Power Electron.*, vol. 21, no. 4, pp. 1032–1040, Jul. 2006.

[15] J. Dannehl, F. W. Fuchs, and P. B. Thøgersen, "PI state space current control of grid-connected PWM converters with LCL filters," *IEEE Trans. Power Electron.*, vol. 25, no. 9, pp. 2320–2330, Sep. 2010.

[16] X. Yuan, W. Merk, H. Stemmler, and J. Allmeling, "Stationary-frame generalized integrators for current control of active power filters with zero steady-state error for current harmonics of concern under unbalanced and distorted operating conditions," *IEEE Trans. Ind. Appl.*, vol. 38, no. 2, pp. 523–532, Mar./Apr. 2003.

[17] T. Abeyasekera, C. M. Johnson, D. J. Atkinson, and M. Armstrong, "Suppression of line voltage related distortion in current controlled grid connected inverters," *IEEE Trans. Power Electron.*, vol. 20, no. 6, pp. 1393–1401, Nov. 2005.

[18] S. Y. Park, C. L. Chen, J. S. Lai, and S. R. Moon, "Admittance compensation in current loop control for a grid tie LCL fuel cell converter," *IEEE Trans. Power Electron.*, vol. 23, no. 4, pp. 1716–1723, Jul. 2008.

[19] J. Dannehl, M. Liserre, and F. W. Fuchs, "Filter-based active damping of voltage source converters with LCL filter," *IEEE Trans. Ind. Electron.*, vol. 58, no. 8, pp. 3623–3633, Aug. 2011.

[20] P. Rodriguez, A. Luna, I. Etxeberria, J. R. Hermoso, and R. Teodorescu, "Multiple second order generalized integrators for harmonic synchronization of power converters," in *Proc. Energy Convers. Congr. Exhib.*, 2009, pp. 2239–2245.

[21] K. H. Ahmed, A. M. Massoud, S. J. Finney, and B. W. Williams, "Sensorless current control of three-phase inverter-based distributed generation," *IEEE Trans. Power Del.*, vol. 24, no. 2, pp. 919–929, Apr. 2009.

[22] M. Xue, Y. Zhang, F. Liu, Y. Kang, and Y. Yi, "Optimized pole and zero placement with state observer for LCL-type grid-connected inverter," in *Proc. Energy Convers. Congr. Expo.*, 2011, pp. 377–382.

[23] J. L. Agorreta, M. Borrega, J. Lopez, and L. Marroyo, "Modeling and control of N-paralleled grid-connected inverters with LCL filter coupled due to grid impedance in PV plants," *IEEE Trans. Power Electron.*, vol. 26, no. 3, pp. 770–785, Mar. 2011.

[24] S. Mariéthoz, M. Morari, "Explicit model-predictive control of a PWM inverter with an LCL filter," *IEEE Trans. Ind. Electron.*, vol. 56, no. 2, pp. 389–399, Feb. 2009.

[25] M. Xue, F. Liu, Y. Kang, and Y. Zhang, "Investigation of active islanding detection methods in multiple grid-connected converters," in *Proc. Int. Power Electron. Motion Control Conf.*, 2009, pp. 2151–2154.

[26] M. Castilla, J. Miret, J. Matas, and L. G. de Vicuña, J. M. Guerrero, "Control design guidelines for single-phase grid-connected photovoltaic inverters with damped resonant harmonic compensators," *IEEE Trans. Ind. Electron.*, vol. 56, no. 11, pp. 4492–4501, Nov. 2009.

Mingyu Xue was born in Zhejiang, China, in 1984. He received the B.S. degree in electrical engineering with automation from the Dalian University of Technology, Dalian, China, in 2006, and the M.S. degree in power electronics and drive from the Huazhong University of Science and Technology, Wuhan, China, in 2008, where he is currently working toward the Ph.D. degree.

His research interests include power electronic converters, renewable energy, and distributed generation.

Yu Zhang (M'11) received the M.S. and Ph.D. degrees in electrical engineering from the Huazhong University of Science and Technology, Wuhan, China, in 1995 and 2005, respectively.

From 1995 to 2002, he was an Engineer with Power Supply Applications. He is currently an Associate Professor in the College of Electrical and Electronic Engineering, Huazhong University of Science and Technology, where he teaches power electronics. His research interests include power electronics modeling and control, parallel UPSs, and renewable energy generation.

Yong Kang was born in Hubei, China, in 1965. He received the B.E., M.E., and Ph.D. degrees from the Huazhong University of Science and Technology (HUST), Wuhan, China, in 1988, 1991, and 1994, respectively.

In 1994, he joined HUST as a Lecturer and was promoted to an Associate Professor in 1996 and to Full Professor in 1998. He is currently the Head of the College of Electrical and Electronic Engineering, HUST. He is the author of more than 60 technical papers. His research interests include power electronic converters, ac drivers, and electromagnetic compatibility techniques.

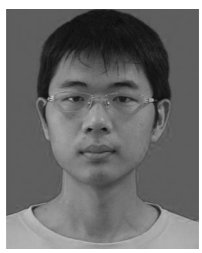

Yongxian Yi was born in Zhejiang, China, in 1988. He received the B.S. degree in electrical engineering from Zhejiang University, Hangzhou, China, in 2010. He is currently working toward the M.S. degree in electrical engineering at the Huazhong University of Science and Technology, Wuhan, China.

His research interests include power electronic converters and renewable energy.

Shuming Li was born in Hunan, China, in 1980. He received the B.S. degree (network) in electrical engineering from the Huazhong University of Science and Technology, Wuhan, China.

Since 1999, he has worked as an Electronic Engineer in Zhicheng Champion Ltd., Guangdong, China, and has been a Principal Designer for several generations of photovoltaic inverter and UPS. He is currently the Project Manager in the R&D Department. His research interest and professional specialities include the low-cost, highly reliable power electronic converters.

Fangrui Liu received the B.Eng. degree in electrical engineering from the Huazhong University of Science and Technology, Wuhan, China, in 2002, and the Ph.D. degree from Nanyang Technological University, Singapore, in 2006.

He joined the College of Electrical and Electronic Engineering, Huazhong University of Science and Technology in September 2006, where he has been a Lecturer since September 2008. He is also a Postdoctoral Fellow with the Department of Electrical and Computer Engineering, Ryerson University, Canada. His research includes power converters, ac motor drives and renewable energy resources.